ROBUST 5G/B5G MILLIMETER-WAVE MIMO COMMUNICATION IN A SPARSE
SCATTERING ENVIRONMENT

A DISSERTATION SUBMITTED TO THE GRADUATE DIVISION OF THE
UNIVERSITY OF HAWAI'I IN PARTIAL FULFILLMENT OF THE
REQUIREMENTS FOR THE DEGREE OF

MASTERS OF SCIENCE

IN

ELECTRICAL ENGINEERING

JULY 2022

By
Willy Chang

Dissertation Committee:

Y. Zheng, Chairperson
Y. Dong
G. Sasaki

Acknowledgements

I would like to thank those who have assisted me during my academic journey in the master's program. This thesis defense would not have been possible without the guidance and the help of several individuals who, in one way or another, contributed and extended their valuable assistance in the preparation and completion of this study.

To my advisor and captain of the HH 488, Dr. Yao Zheng, thank you for your continual guidance throughout my graduate career. It was a pleasure spending the long hours figuring out the issues with our setup, listening to your endless, in-depth knowledge of Star Trek, and watching digital animations together.

To the committee members, Dr. Galen Sasaki and Dr. Yingfei Dong, thank you both for your insightful comments and suggestions throughout my defense. I am both honored and glad you two were able to serve on my committee to top off the years of academic courses I shared with you.

To my fellow colleagues, Saige Dacuycuy, Denny Landika, and Zachary Dela Cruz, thank you for your steadfast presence and motivation in and outside the lab. It was a delight to have people whom I could bounce ideas around and reinforce the knowledge I had in the field. I would also like to extend my thanks to the many undergraduate students I worked with throughout my graduate career. Special thanks to PhD student, Khaldoon Ishmael, for all the advice you provided me.

To my dear friends, specifically Anne Mo, Nanako Nishiyama, and Shelley Yang, whom have been by side for the last decade, thank you for your steadfast presence and calming voices of reason. All my worries and troubles would melt away during our conversations,

and I cherish every moment we spent together, and look forward to every moment in the future together.

And last but not least, to my family, for always being there unconditionally and giving me the unending freedom to pursue my passion, thank you. To my father, Seaton Chang, thank you for working many hard hours to provide for the family and sharing moments of laughter during our brief conversations alone. To my elder sister, Milly Chang, thank you for being a trailblazer, watching over and guiding me with your wealth of experiences. To my youngest sister, Juliana Chang, thank you for supporting me ever so silently in the background. To my mother, Mina Chang, thank you for persistently telling me to never give up and to do the best that I can. I cannot express in words how much I appreciate your endless love that sustained me through difficult times. Thank you so much.

Abstract

Wireless sensing and communication is heading into a new era with the advent of fifth generation (5G) capabilities. Although these higher frequency bands are expected to increase throughput and reduce latency to meet increasing mobile user demands, they face significant challenges due to changes in physical characteristics that require different solutions compared to existing methods. One such method is multiple-input, multiple-output (MIMO), a way to increase the capacity of a communication link by exploiting multipaths that exist in the environment. While this rich scattering environment provides the diversity required, at mm-Wave, such paths are non-existent as a consequence of the rapid attenuation shorter wavelengths experience and blockages that prevent the signal from propagating through them. To support MIMO operations, existing research opt to focus on line-of-sight (LoS) MIMO to ensure an orthogonal channel matrix. However, these optimizations are unfeasible over longer distances and limited separation distances for both the transmitter and the receiver. We investigate the non-LoS (NLoS) channels via reflectors as an alternative to a LoS link for a robust procedure in maintaining the communication link. Several preliminary ideal simulations of the channel matrix under 2x2 and 3x3 MIMO were implemented to identify key areas of interest for antenna elements to guide their transmitted singal in order to maximize the channel capacity. We also conducted real-world experiments at 28 GHz to demonstrate that the measured channels are in good agreement with the theory for NLoS MIMO. We also conduct a theoretical analysis of the time complexities for potential path finding and path selection algorithms that leverage the given information to achieve the best possible throughput while minimizing overhead.

Table of Contents

List of Tables

List of Figures

x

Chapter 1

Introduction

In this section, we introduce a high level overview of the current environment surrounding 5G and MIMO that will serve as the backdrop into the discussion for the need to have robust millimeter-wave MIMO communication in a sparse scattering environment. It will cover descriptions on the 5G spectrum, MIMO, and the motivation behind the thesis.

1.1 Foundation

Nowadays, there is an indisputable need to equip existing technology with the ability to meet ever-increasing mobile user demands. In the very last quarter of this year, global mobile device website traffic consisted of 58.99% of all web traffic, an almost 30% increase in past 7 years [1]. Applications, too, are demanding higher bandwidth requirements for activities such as ultra high-definition videos and virtual reality, not to mention other activities like multiplayer gaming, music streaming, and video calling. In order to satisfy these requests across different users, 4G LTE will not be sufficient. Herein lies the current rollout of technology, sub-6 GHz. This is a convenient frequency range because it overlaps with the LTE 4G spectrum, making it easier to modify existing systems to accommodate the change while simultaneously seeing improvements in bandwidth and coverage speeds. While sub-6 GHz offers these benefits, it's similarity to the generation before it means that the capacity of these systems are still limited with a congested spectrum and limited bandwidth. To resolve

these restrictions, there are two improvements that can be made that are key technologies for 5G/B5G: (1) millimeter waves and (2) massive multiple input, multiple output (MIMO).

1.2 Understanding 5G

With the full release of the fifth generation (5G) new radio (NR) Release 15 (Rel 15) standards by the 3rd Generation Partnership Project (3GPP) in 2017 [2] and corresponding technical advances in software and hardware devices, the integration of these higher frequency bands in everyday communication devices is becoming closer to reality to expand upon current capabilities. The delivery of these specifications extends upon previously existing Rel 15 instructions for integrated 5G and LTE (Long-Term Evolution) radio systems to enable standalone 5G radio systems. With 5G systems, many fields including telecommunications and healthcare seek to realize peak potential peak data rates of up to 20 gigabits per second (Gbps) and broader bandwidths up to 1 GHz based on IMT-2020 requirements to support ever increasing mobile user demands in a quantity-limited availability of the electromagnetic spectrum.

1.3 5G/5G-NR Frequencies

The fifth generation of wireless technology incorporates frequency bands from 700 MHz up to 100 GHz. This wide-range is further separated into two distinct bands known as sub-6 GHz and millimeter-wave (mmWave) frequencies, each characterized with their own unique features and properties that impact the methods and support needed to maximize their effectiveness in applications.

1.3.1 Sub-6 GHz

The lower to middle band of the 5G spectrum, sub-6 GHz covers frequencies less than 6 GHz. More specifically, it describes the region of signals between 700 MHz and 6 GHz, where the lower band occupies the frequencies from 700 MHz to 2 GHz and the middle band

occupies the rest of the spectrum from 2 GHz to 6 GHz. The lower range overlaps with existing 4G LTE frequencies, exemplifying the similarities between the two while offering marginal improvements in latency and throughput. Due to the comparable nature of 4G and sub-6 GHz, current deployments of 5G interfaces commonly use the n78 band operating at 3.5 GHz to capitalize on the extended coverage and unused spectrum that the band offers. Dictated by the wavelength formula. These radio frequencies measure in centimeters (cm), giving the spectrum the name of centimeter-band or centimeter-wave frequencies.

1.3.2 Millimeter-Wave

The millimeter-wave spectrum resides at higher frequencies, typically in the range between 24 to 100 GHz. The benefits of this As the name suggests, the wavelengths of signals residing in this band are measured in millimeters (mm). These signals can be used to capture more information over the same distance because of their shorter wavelengths. In a full duplex communication scheme, both parties in the communication link are able to transmit and receive at the same time. Time-division duplexing (TDD) applies the concept of time-division multiplexing for the uplink (UL) and downlink (DL) signals to emulate full-duplex functions. TDD operates at the same frequency band, but separates the UL and DL process via time (i.e. at time t_0, the UL signal is sent and at time t_1, the DL signal is sent). Assuming that the speed of the data stream remains is the same, over the same period of time, the signal with a shorter wavelength will both be faster and have greater throughput. Alongside the fact that the region is largely unoccupied and has a greater potential for larger bandwidth operations, applications can leverage this spectrum to resolve bandwidth limitations present at sub-6 GHz and below [3].

1.4 Multiple Input, Multiple Output

MIMO is an essential method in radio communication that exploits the multiple transmission paths (multipaths) to increase the capacity of communication links between

multiple transmitters (TX) and multiple receivers (RX) [4, 5, 6]. In this paradigm, parallel data streams are transmitted and received concurrently to maximize the gain on the downlink. This is accomplished when the channel vectors composed of the channel state information (CSI) on the receiver end are orthogonal to one another, ensuring a channel rank identical to the number of spatially multiplexed data streams for independent separation of transmitted information. The CSI defines the transmission path characteristics, encompassing information that describes how the signal propagates from the transmitter through the environment to the receiver, including the combined effects of parameters such as fading, scattering, and attenuation. This information is usually estimated at the receiver using known pilot symbols at both ends of the telecommunication link [7]. Ensuring separability of concurrent data transmissions extends capabilities to communicate with multiple users simultaneously.
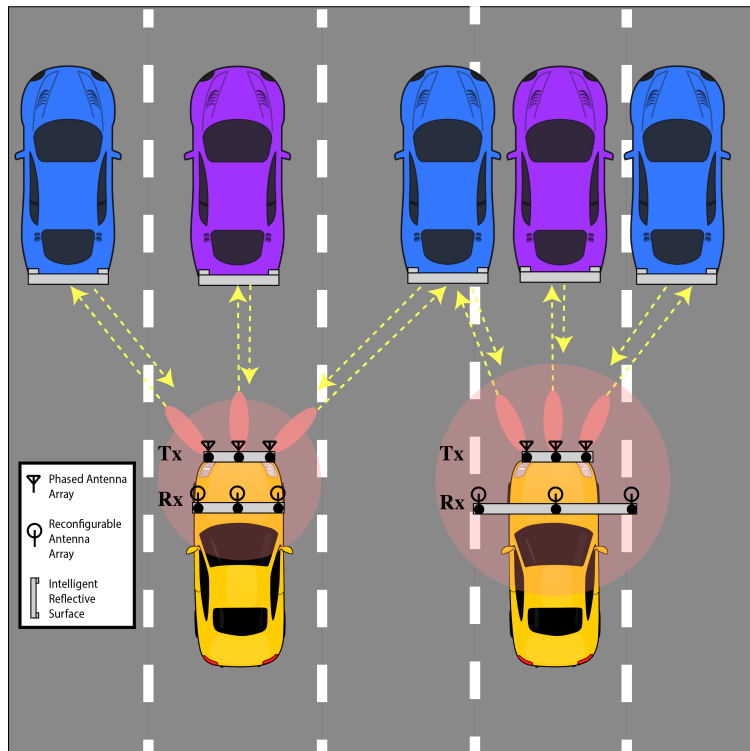
Figure 1.1: V2V communication limitation.

1.5 Motivation

Despite the advantages that mmWaves and MIMO provide to seemingly resolve all the issues in a congested, narrow bandwidth and the need to serve numerous users at the same time, there exist disadvantages, conjuring up a host of new problems that require solutions prior to commercial implementation.

In the case of mmWaves, the spectrum faces has significant challenges. One such challenge is the path loss (PL) that frequencies at that magnitude experience as it travels from one point to another, as dictated by the simplified Friis' free-space path loss (FSPL) formula [8]

$$FSPL = (\frac{4\pi df}{c})^2$$

where d is the distance between two points, f is the carrier frequency of the signal, and c is the speed of light constant. The formula assumes that the target is in the far-field of the transmitting element, assuming that electromagnetic radiation behavior dominates over reactive, non-radiative behavior observed when the distance is below a wavelength of the signal. For a every unit distance, the path loss increases by a magnitude of 10 for higher-band signals compared to those at sub-6 Ghz. Expressing the path loss in decibels, we can apply the logarithmic function to the FSPL, and with some algebraic manipulation, the formula obtained is

$$FSPL \, (\text{dB}) = 20log \, (d) + 20log \, (f) + 20log \, (\frac{4\pi}{c})$$

A magnitude increase in frequency corresponds to a 20 dB gain in the path loss. For a complete picture of the equation, the antenna gains at the transmitter and receiver need to be incorporated. The final result is as follows

$$FSPL \, (\text{dB}) = 20log \, (d) + 20log \, (f) + 20log \, (\frac{4\pi}{c}) - G_{TX} - G_{RX}$$

5

where G_{TX} and G_{RX} are the antenna gains from the transmitter and receiver, respectively. Consequently, the PL nature of mmWaves requires beam-forming solutions to concentrate the power of multiple antennas in a certain direction, establishing the ability to steer the radio frequency (RF) signal and ensure a high signal-to-noise ratio (SNR). The superposition of multiple antennas in unison focus the energy of the generated signal in a particular direction to allow the signal to travel further link distances.

In the case of MIMO, the method requires multipaths to enable spatial diversity. These multipaths are not as prevalent at mmWaves because of another property of mmWaves: the propensity to be obstructed by a variety of obstacles including cars, trees, buildings, and people [9]. The short wavelengths of these signals tend to scatter more than those of longer wavelengths when colliding with other objects. Combined with the severe attenuation mmWaves experience over longer distances, the number of reflective paths experienced at the receiver is not as rich and diverse as those that can be found at sub-6 GHz frequencies [10].

To combat these issues, techniques such as massive MIMO, or large scale antenna systems, and line-of-sight (LoS) mmWave MIMO play large roles. In massive MIMO, many antenna elements are combined together to create a stronger beam, focusing the power of the combined signal in a particular direction [11, 12]. This is possible because the shorter wavelengths at mmWaves correspond to smaller antenna elements that can be packed together in a phased array format.The technology falls under the category of multi-user MIMO (mu-MIMO) systems and seeks to carry out multiplexing on base stations (BS) with a large number of antenna elements to improve spectral and energy efficiency. It leverages the scalability of the base station to have an antenna count much greater than the number of users, and requires the frequency response of the propagation channels from each antenna element to the user-endpoint (UE) to be known at the BS. LoS MIMO is a certain kind of MIMO that focuses on the line-of-sight propagation path. The benefit of doing so is that the LoS path is the direct, point-to-point path from the transmitters to the receivers, thus having the least amount of path fading. In order to maintain orthogonality

6

of the channel matrix, an optimal geometric placement of the antennas is necessary and described in the equation known as the Rayleigh criterion or Rayleigh spacing.

When talking about mmWave MIMO, most of the literature focuses on the LoS, optimizing the spacing of the antennas according to Rayleigh's spacing [13, 14, 15]. However, that equation is restrictive and unsuitable for communication over longer distances. As the distance between your antenna arrays becomes larger, a greater distance between antennas in the arrays is needed in order to maintain the optimal spectral efficiency of the communication link. This is not possible when you have a limited area to work with in placing your antenna arrays, such as in vehicular-to-vehicular (V2V) communication. This work looks at the potential of mmWave MIMO using non-line-of-sight paths, which offers the capability to circumnavigate blockages that may exist in the line-of-sight path and to determine if MIMO capabilities can be achieved in constrained spaces.
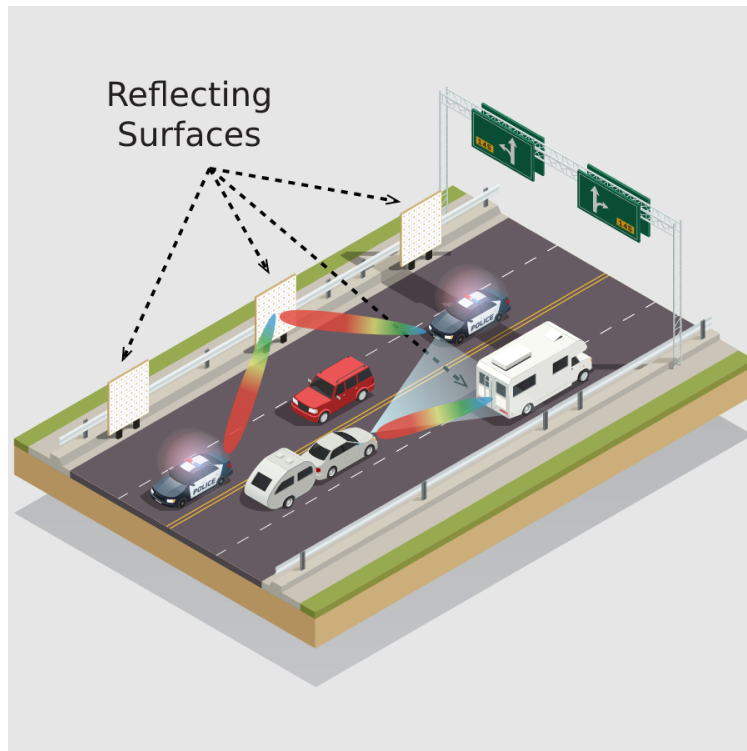
Figure 1.2: V2V NLoS path.

These NLoS paths can be constructed to address these coverage issues with cost-efficient extension devices, such as as relay antenna arrays and repeaters. More recently, devices known as intelligent reflecting surfaces (IRS), re-configurable intelligent surfaces (RIS), or meta-surfaces retain the ability to control the reflection pattern and resonant frequency of an incoming signal [16, 17, 18, 19]. The captured signal is then re-radiated towards other APs through passive or active reflection, depending on the elements of these reflective surfaces, offering greater precision in guiding the signal towards the intended recipient as opposed to a typical metal surface.

1.6 Outline

The rest of this thesis is organized as follows. Chapter 2 provides further background information on related areas, formally presents the problem mathematically, and provides a theoretical implementation of path finding and path selection algorithms. Chapter 3 presents the methodology of the simulation and experimental testbed. Chapter 4 describes the results, related work, and discussions. Chapter 5 concludes the thesis, summarizing the contributions of the thesis to the field of integrated sensing and communication and future work.

Chapter 2

Background Information

In this section, we provide a technical introduction into , defining the channel model, the Rayleigh criterion, and related metrics that will be evaluated in the rest of the paper. It will also define the problem of using NLoS multipaths for mmWave MIMO in a formal manner.

2.1   Channel Model

(a) General MIMO setup.

(b) 2x2 MIMO.
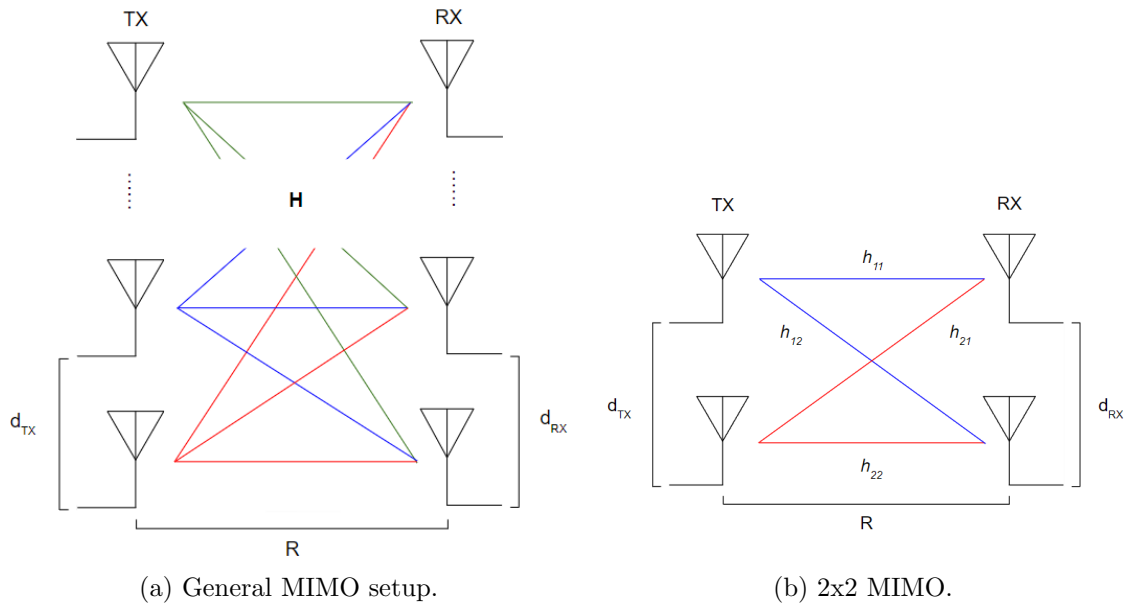
Figure 2.1: Multiple input, multiple output.

To properly define the LoS channel model, consider a time-invariant N_{TX} by N_{RX} complex deterministic channel matrix $\mathbf{H}$ that defines the LoS MIMO channel environment seen in Figure 2.1a expressed as follows

$$\mathbf{H} = [\mathbf{h}_1, \mathbf{h}_2, \ldots, \mathbf{h}_{N_{TX}}]^T$$

where it is composed of individual LoS multipaths $\mathbf{h}_i$ vectors from transmitter i to N_{TX} receivers, and can be represented as

$$\mathbf{h}_i = [h_{i,1}, h_{i,2}, \ldots, h_{i,N_{RX}}]$$

where $h_{n,m}$ denotes the CSI from transmitter n to receiver m. Each LoS component is theoretically given as

$$h_{n,m} = a_{n,m}\exp(-j2\pi\frac{r_{n,m}}{\lambda})$$

with $a_{n,m}$ being the attenuation coefficient depending on the link distance and the gains of the n transmitter and m receiver chains and $r_{n,m}$ being the distance between the n transmit antenna and m receiver antenna. As the LoS is not always at a 0 degree AoD (Figure 2.2), the LoS component can be further decomposed in the following equation

$$\mathbf{h} = a\exp(-j2\pi\frac{d}{\lambda}) \begin{bmatrix} 1 \\ \exp(-j2\pi d_{TX}\cos\theta) \\ \exp(-j2\pi 2 d_{TX}\cos\theta) \\ \vdots \\ \exp(-j2\pi(N_{TX}-1)d_{TX}\cos\theta) \end{bmatrix}$$

where d_{TX} is the distance between transmitter antennas and θ is the angular displacement of the LoS path.

As the transmitter and receiver antennas are positioned at an angle θ_i, where i is the number of beam-steering angles, the attenuation coefficient and the effective distance

between the transmitter and receiver will change depending on the length of the resulting transmission path, and the relationship between the distance and the attenuation coefficient is inversely proportional to one another.
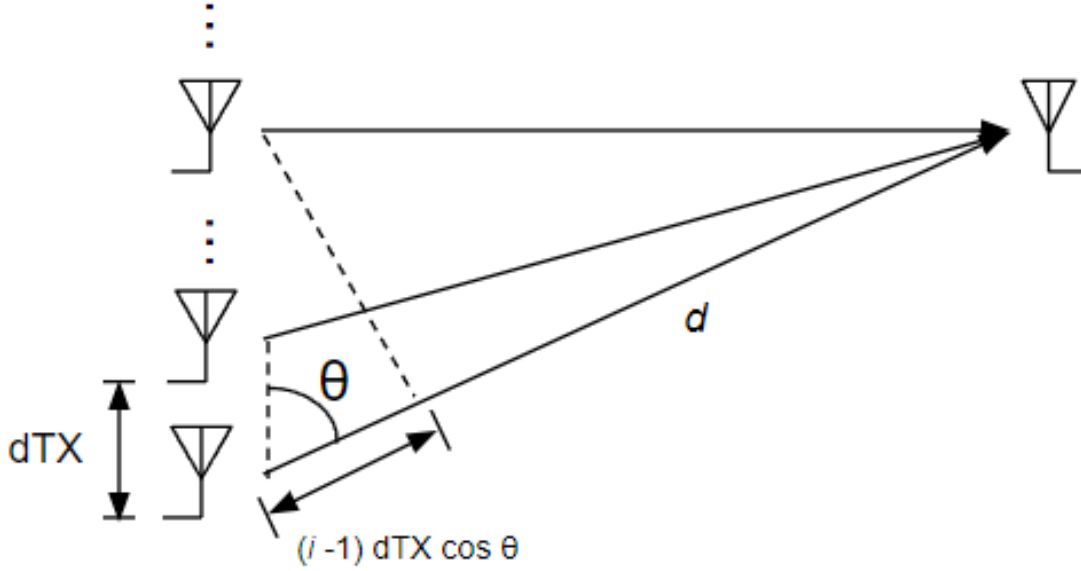
Figure 2.2: LoS channel with multiple transmit antennas and a single receive antenna.

To further describe the correlation between the beam-steering angle θ_i and the components in the channel matrix, let there be a function $\mathbf{f}_t(\theta)$ that defines the spatial signature in the directional angle θ_i for the transmitters to a single receiver, such that

$$\mathbf{f}_t(\theta) = \begin{bmatrix} 1 \\ \exp(-j2\pi d_{TX}\cos\theta) \\ \exp(-j2\pi 2d_{TX}\cos\theta) \\ \vdots \\ \exp(-j2\pi(N_{TX}-1)d_{TX}\cos\theta) \end{bmatrix}$$

We also define a similar spatial signature for the multiple receiver antennas $\mathbf{f}_r(\theta_i)$. The channel matrix, $\mathbf{H}$, can now be represented as

11

$$\mathbf{H} = \sum_k a_k \exp(-j2\pi \frac{d^{(k)}}{\lambda}) \mathbf{f}_t(\theta) \mathbf{f}_r(\theta)$$

for multiple transmitters and multiple receivers, where k is the path number for the various multipaths.

The resulting received signal of the channel can now be described by

$$\mathbf{y} = \mathbf{Hx} + \mathbf{w}$$

where $\mathbf{x} \in \mathbb{C}^{N_{TX}}$ is the transmitted signal, $\mathbf{y} \in \mathbb{C}^{N_{RX}}$ is the received signal, and $\mathbf{w} \sim \mathcal{CN}(0, \sigma^2 \mathbf{I}_{N_{RX}})$ is a noise vector with a random circular symmetric complex normal distribution. $\mathbf{I}_N$ is the identity matrix with dimension N. This particular model assumes synchronization of the frequency offset between the transmitter and the receiver (i.e. shared reference clock generator).

2.2 LoS mmWave MIMO

In the direct LoS mmWave MIMO, the channel characteristics that significantly influence and determine the orthogonality of channel vectors lies with the antenna spacing and distance. The geometric spacing of the antennas ensure that interference from one data stream does not result in a destructive superposition of signals, but a constructive inference for a power gain of the received multiplexed channels. This spatial optimization is defined through the Rayleigh spacing criterion as defined [5, 20, 21]

$$d_{TX} d_{RX} = \frac{R\lambda}{N_{RX}}$$

The criterion defines the linear relationship of the distances between transmitters (d_{TX}), the distances between receivers (d_{TX}), the wavelength of the carrier signal λ, and the distances between the transmitters and receivers (R), where N_{RX} is the number of receivers.

2.2.1 Metrics

After characterizing the channel model and the channel matrix, we can now look at the metrics that can help us determine the efficacy of communication link. The values we observe are the channel capacity and the condition number. The channel capacity is the rate at which information is reliably transmitted, and is defined as follows:

$$\arg\max_{\theta_i} \; log(det(\mathbf{I}_N + \rho\mathbf{HH}^H))$$

where $\mathbf{I}_N$ is an identity matrix of N TX antenna elements by N RX antenna elements, ρ is the average signal-to-noise ratio (SNR), $\mathbf{H}$ is the channel matrix, and $\mathbf{H}^H$ is the hermitian of the channel matrix. For this measure, the higher the channel capacity, the better as more information can be obtained from the channel.

It is worth noting that $\mathbf{H}$ can be represented as a function of θ_i. With some algebraic manipulation, we further decompose the optimization problem below:

$$C = \log(det(\mathbf{I}_N + \rho(\sum_k a_k \exp(-j2\pi\frac{d^{(k)}}{\lambda})\mathbf{f}_t(\theta_i)\mathbf{f}_r(\theta_i))(\sum_k a_k \exp(-j2\pi\frac{d^{(k)}}{\lambda})\mathbf{f}_t(\theta_i)\mathbf{f}_r(\theta_i))^H)$$

but for simplicity, we reference the equation using the channel matrix, $\mathbf{H}$.

The condition number, κ, is a measure of how much the output changes given changes to the input, and can be calculated by finding the maximum eigenvalue of the matrix and dividing it by the minimum eigenvalue of the channel matrix [22].

$$\kappa = \frac{\lambda_{max}(\mathbf{H})}{\lambda_{min}(\mathbf{H})}$$

This metric gives us an idea on the orthogonality of the channel matrix, and how well the concurrent data streams can be separated. A well-conditioned matrix has lower condition numbers with the best being 1.

13

2.3 Defining the Problem

For point-to-point mmWave MIMO, as mentioned previously, has extensive research conducted on the optimal spacing of antenna elements. However, this methodology is not suitable for long-range communication or under constrained placement of the antenna elements. Consider vehicular to vehicular (V2V) or virtual reality (VR) applications where the amount of space to place equip multi-antenna systems is limited and the dynamic nature of the situation is unsuited to consistently maintain the optimal geometric spacing identified in Rayleigh's spacing criterion, necessitating a solution to account for such situations. The thesis presents simulations pertaining to the given limited spatial placement of the transmitters and offers situations leveraging the potential amplitude and phase modulations that can be provided through reflectors, identifying areas of interest to prevent channel correlations.

The problem can be formally defined as a constrained optimization problem to maximize the channel capacity C. The tuning argument or inputs is the

$$\arg \max_{\theta_i} \; log(det(\mathbf{I}_N + \rho \mathbf{H} \mathbf{H}^H))$$

where θ_i is the set of AoD for each TX antenna beam and the AoA for the RX antenna beam.

We further sub-divide the optimization problem into two portions: (1) considering the given channel matrix and (2) investigate only the phase differences of the elements by applying a normalization to the matrix, like below.

$$(\mathbf{H}_{\text{norm}})_{nm} = \frac{\mathbf{H}_{nm}}{|\mathbf{H}_{nm}|}$$

2.4 Path Detection

Armed with simulation graphs and reinforced with real-world measurements in the upcoming sections, the information provided can be utilized to assist in identifying optimal

paths for transmitter beams during their sweep. We discuss the naive solution in an exhaustive search, offer an alternative that takes advantage of the coverage map to optimize a random search algorithm, and discuss a compressed sensing algorithm.

2.4.1 Exhaustive Search

Let us first define the comparative benchmark to isolate the dominant paths that lead to high SNR communication link in the MIMO system. For concurrent transmission of m data streams across N beam-steering positions, there are N^{2m} possible beam combinations [23]. The worst-case time complexity of this method is the same for the average case under the same assumptions.

2.4.2 Random Search

In a random search implementation, the worst-case search space is identical to the naive method. However, the simulations and experiments indicate that optimizations can be made with prior information regarding the regions where NLoS paths have a higher probability of fulfilling the Rayleigh criterion and produces a well-conditioned matrix. In other words, for a certain direction N, a deterministic probability can be assigned to it, where the probability follows the a priori hyperbolic field distribution that lead to well-conditioned matrices. Although the specific probability depends on the antenna array pattern, assuming a non-zero expectation, the average case reduces down to $O(\mathrm{E}[N]^{2m})$.

2.4.3 Compressed Sensing

Another alternative to the two methods mentioned above is a compressed sensing algorithm discussed in Xie et al [24]. In the compressive estimation scheme, the method utilizes a constant number of composite CSI measurements to determine the dominant signal paths. This is possible due to the sparse nature of mmWaves, where the AoA distribution is clustered into 3-5 distinct directions. Coupled with the prior knowledge provided by

15

a relatively constant coverage map to determine the directions of encountering a higher channel capacity, we can further improve the architecture of detecting optimal paths.

2.5   Path Selection

While numerous algorithms could be used to select the appropriate path that would provide separability of data streams among the candidate paths detected in the previous section, the one recommended here is a simple graph coloring algorithm [25, 26]. In this situation, the vertices represent distinct paths between a transmitter and a receiver, and the edges represent correlated paths between vertices.

Chapter 3

Methodology

In this section, we provide an in-depth description pertaining to both the hardware and software used for the simulation and the experiments.

3.1 Experimental Platform

In the exploration of the potential to use non-line of sight paths as an alternative to the desired LoS method under spatial constraints for the n257 band (i.e. Local Multipoint Distribution Service (LMDS)) [2], a series of experimental simulations and real-world experiments were conducted. The following sub-sections discuss the setup for the simulation and testbed, respectively.

3.1.1 Simulation Framework

Preliminary results were obtained via simulation primarily using the numeric computing environment, MATLAB. The program was installed on a Lenovo ThinkServer RD330 equipped with two (2) Intel(R) Xeon(R) CPU E5-2430 0 @ 2.20 GHz, 4 TB of free storage space, 128 GB of RAM, and operating on Ubuntu 20.04.3 LTS. Due to the lack of a graphical interface on the server, the Bourne script used to launch the program was installed alongside the `-nodisplay` option, the Parallel Computing Toolbox, the Phased Array System Toolbox, and related supporting toolboxes. The Parallel Computing Toolbox lets MATLAB execute

applications on multicore processors, GPUs, and computer clusters through parallel-enabled functions. This functionality is crucial to accelerate the computations conducted for the simulations. With 12 parallel workers, the toolbox enabled approximately 2,800 cells to be computed per second. The Phased Array System Toolbox provides algorithms to simulate sensor array and beamforming systems in a multitude of applications including wireless communication. This additional capability is a main component in the simulation of the communication link in the scenario presented for path selection.

3.1.2 mmWave Measurement Testbed

The measurement setup consists of three subsystems all equipped on a mobile computer rack that will be described in the next three subsections. The simplified schematic for the setup can be seen in Figure 3.1a and the system setup is shown in Figure 3.1b.
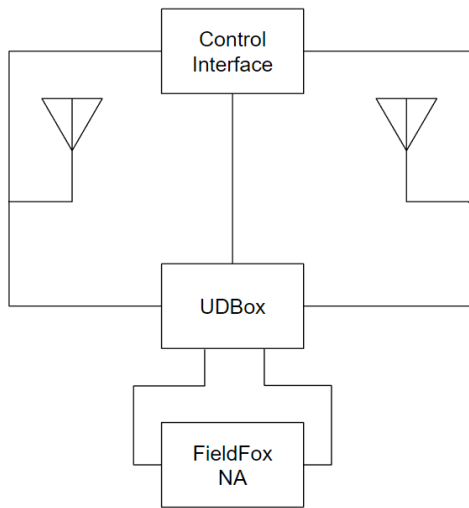
(a) Testbed schematic.
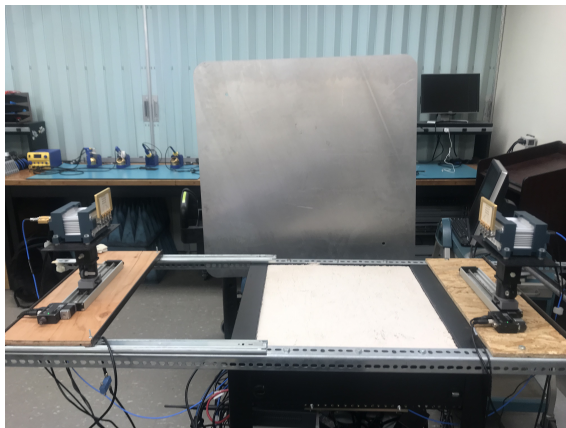
(b) Testbed.

Figure 3.1: Testbed setup.

In conducting NLoS measurements, the beamformers would be steered towards the direction of a metal reflector, which would reflect the signal from the angle of incidence according to Snell's law. Due to the setup's pre-existing beamsteering abilities, the physical orientation of the beamformers themselves required no change.

18

3.1.3   Signal Generation and Reception

The first subsystem consists of the signal generation, recording procedure, and related devices. A Keysight FieldFox Microwave Analyzer N9918A is a portable, handheld analyzer equipped to analyze signals on the spectrum from 30 kHz to 26.5 GHz. Capable of operating as a cable and antenna analyzer (CAT), a vector network analyzer (VNA) and a spectrum analyzer (SA), the device serves as the baseband signal generator as well as an analyzer for the received signal. The baseband test signals delivered through the channel are generated using the VNA functionality, creating a sweeping tap signal response of 10 MHz in the span and power level specified on the device. The received signal is then captured on the receiving port of the FieldFox, where the scattering (S) parameter is measured. The FieldFox is controlled using a MATLAB script connected to the device via TCP/IP. This method allows recording of traces from the analyzer to measure of the S-21 parameter (i.e. forward transmission coefficient).

The S-21 is a scattering parameter that represents the linear electrical characteristics of the signal received at port 2 from port 1 in a two-port network. From this measurement, two properties are extracted: the scalar logarithmic gain and the phase of the received signal. Let the S-21 parameter complex linear gain G be defined formally as

$$G = S_{21} = \frac{y}{x}$$

where y is the power wave entering from port 2 and x is the incident power wave at port 1, where traditionally b_2 and a_1 are used for y and x, respectively. With this definition, we can draw equivalencies to the CSI and the linear solution for the channel matrix $\mathbf{H}$. As such, the desired CSI can be obtained as a complex combination through the scalar linear gain (i.e. magnitude), which is the absolute value of the complex linear gain, and the phase of the S-21 parameter.

3.1.4 Conversion of Generated Signal

The second subsystem is made up of radio frequency (RF) cables, coaxial cables, and a TMYTEK UD Box 5G. The UD Box is a dual channel up/down converter comprised of mixers, intermediate frequency (IF) and RF filters, and an internal local oscillator (LO) built using a phase-locked oscillator (PLO) as seen in the diagram in Figure 3.2a used to convert the baseband, centimeter-level frequencies to the desired n257 mmWave, carrier band frequencies. The up/down converter has an operational RF frequency range of 24 to 44 GHz and an IF frequency range from 0.01 to 14 GHz with an adjustable LO frequency of 16 to 32 GHz.
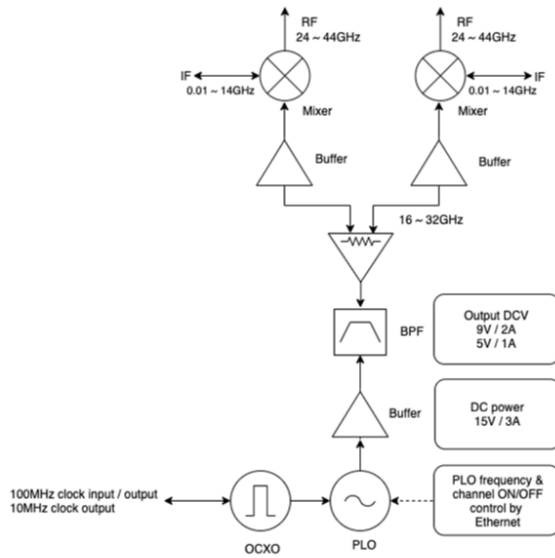
(a) UD Box block diagram.   (b) Actual UD Box.

Figure 3.2: Up/Down Converter.

In the testing setup, the generated baseband signal at 2.4 GHz is up-converted to 28 GHz through the LO via low-side injection of 25.6 GHz with a bandwidth of 50 MHz. At the second port in the dual-channel device (i.e. IF2 and RF2), the signal is down-converted in a mirrored fashion from the up-conversion; that is, the signals frequency is reduced from 28 GHz to 2.4 GHz. The up/down-converter is necessary due to the upper limit of covered

frequencies the FieldFox can handle (26.5 GHz), a range that is just below the 5G n257 frequency band.

3.1.5 RF Front-End
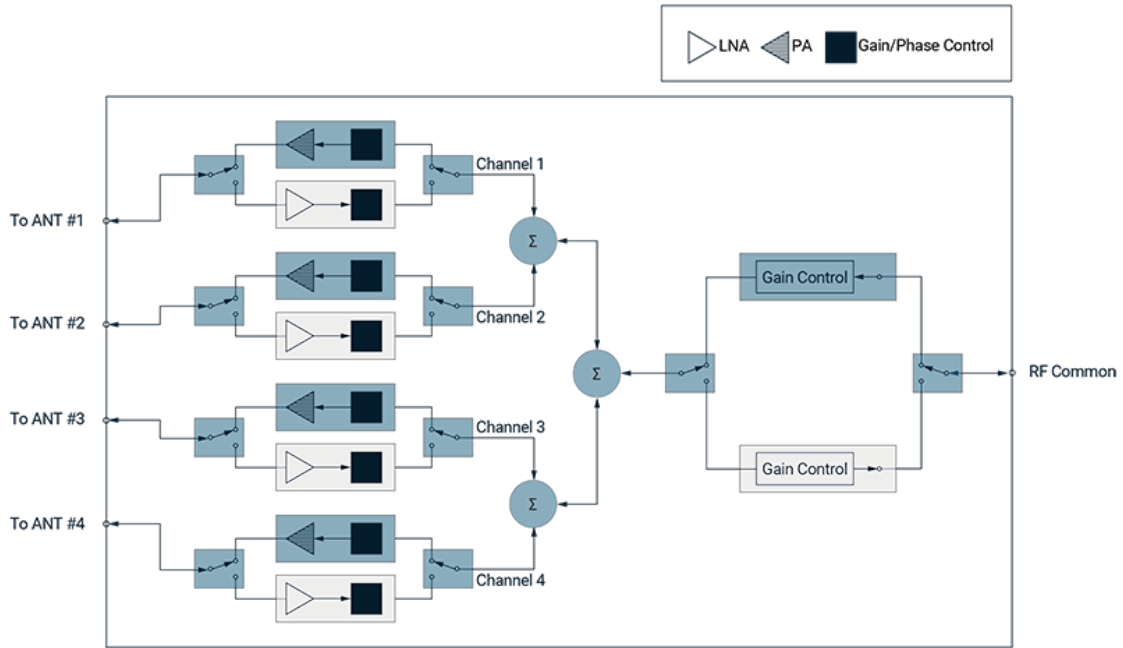
Figure 3.3: BBox Lite 5G block diagram.

The last subsection in the testbed setup consists of two (2) BBox Lite 5G 28 GHz beamformers and two (2) Zaber LHM series 200mm motorized linear stages. The BBox Lite, whose schematic can be seen in Figure 3.2a, is a compact, 4 RF channel controllable 16 element patch antenna designed to operate at the n257 band from 26.5 GHz to 28 GHz. With the ability to not only produce a stronger beam through superimposing the signals from the four RF channels, but also capable of steering the angle of departure (AoD) and the angle of arrival (AoA) of the beam. This particular model can steer the beam from -45° to 45° horizontally, and each channel can be manually configured up to a 360° phase shifter coverage in 5° increments. One BBoxLite (SN: B19138000) is set as the transmitter and the other device (SN: B19483200) is set as the receiver for half duplex operation. The phased arrays are set facing each other (i.e. one at 0° azimuth and the

other at 180° azimuth, respectively), each at a 0° elevation. The configuration and beam-steering of the beamformers are operated using an independent software application called TMYTEK BBox Lite (Figure 3.4b). The software requires a USB connection to each of the BBox Lite devices.
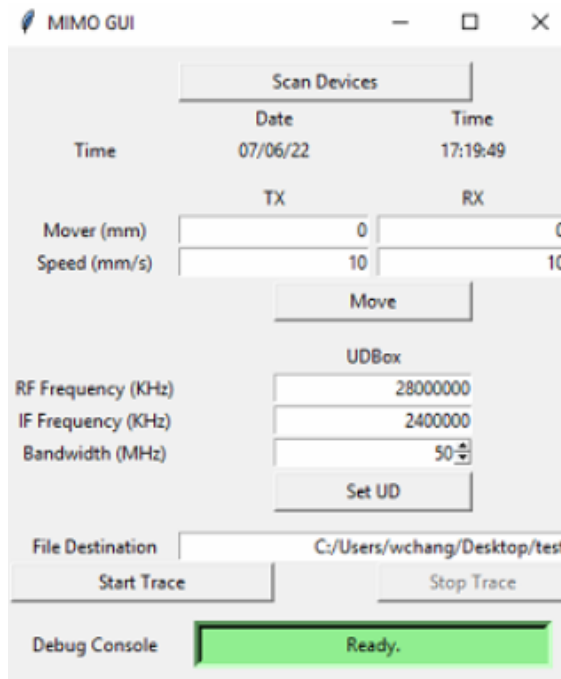
(a) Stage and UD Box control interface.
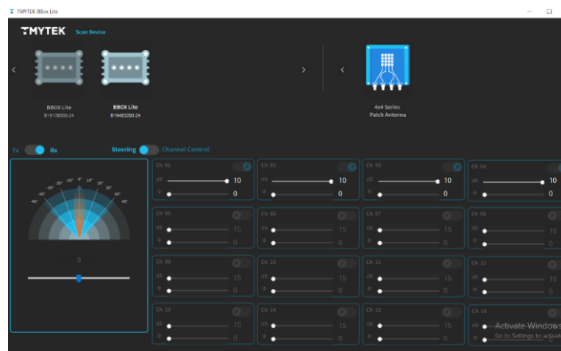
(b) BBox Lite 5G control.

Figure 3.4: Testbed control.

The linear stages offer a controlled displacement environment to take precise measurements on the locations of the transmitting and receiving beamformers while they

propagate the mmWave signal over-the-air (OTA). With the beamformers mounted onto the stages using 3D printed supports, the range of motion for stages go up to around 200 mm with a max speed of 65 mm/s, resulting in a maximum distance of approximately 7 m between arrays for optimal Rayleigh spacing. These stages are controlled using an in-house developed, integrated control interface software created using `tkinter`, `zaber-motion`, `pythonnet`, `numpy`, and `pandas` libraries. The Python code also sets up and controls the UD Box, and is capable of recording the real-time positions of the beamformers in milliseconds (ms). The GUI can be seen in Figure 3.4a.

Chapter 4

Results and Discussion

In this section, the results of the simulation and the testbed are evaluated, the impact of the results are discussed, and an examination towards existing literature is presented.

4.1 Simulation Results

The following subsections discuss the setup of the different simulations explored and a qualitative analysis on the implications of the results for utilizing NLoS mmWave MIMO. As mentioned previously, both the metrics for the calculated channel matrix were calculated as is and a normalization of the matrix were used.

4.1.1 Setup

Under the MATLAB simulation, the 2x2 and 3x3 MIMO situation were explored, both operating at 28 GHz and a sample rate of 8 kHz. A signal with a magnitude of 1 and a phase of 0, a known magnitude and phase, is transmitted and propagated through free space using the free space environment from the `phased.FreeSpace` System object, traveling from a transmitter to each of the receivers in a straight line, the LoS path. The `phased.FreeSpace` object applies a range-dependent time delay, gain, and phase shift to the input signal. For simplicity, the simulation operates under the assumption of motionless APs. The pencil-like beam is suitable for the given situation due to the usage of beamforming capable at mmWave

frequencies. Furthermore, a scatter was present at multiple positions on a horizontal plane containing the antenna elements where one of the transmitter signals would scatter off of and be redirected towards the array of receivers.

In the 2x2 case, to properly emulate and predict real-world measurements from the experimental testbed, the transmitters and receivers were placed 1.0 m apart. To ensure the Rayleigh criterion was met, the receivers were placed approximately 0.073 m apart from each other. One of the transmitters was placed in a fixed position at 0 mm and the other transmitter moved in a linear fashion starting from the first transmitter position up to around 0.073 m, arriving at an approximate position of the Rayleigh criterion on the receiver side. The signal sent from the transmitter traverses through the space towards the all of the respective receivers. The moving transmitters signal is directed towards a reflector at every position in a certain field surrounding the positions of the antennas. The channel matrix is constructed using each of the complex output at the destination. To observe the range effects of the NLoS path, the antenna arrays were fixed at antenna spacings of 0.073 m (e.g. optimal distance between antenna arrays is 1 m) and varied the distances between antenna arrays.

The 3x3 simulation follows a similar procedure, but the third transmitter is at a fixed position in agreement with the optimal antenna spacing and the antenna elements were placed approximately 0.060 m apart in accordance with the increase in the number of antenna elements. The first scenario places two of the transmitters under ideal spacing conditions of a uniform linear array (ULA) at a fixed position on the outer boundaries. The middle transmitter moves from one of the fixed transmitters to the other while capturing the reflective path calculations in the given field. The second scenario, again, fixes the antenna spacings at both APs, but varies the distances between the antenna arrays.

4.1.2 Validation

The accuracy of the simulated model was tested by initially placing the fixed transmitter (TX0) and receivers at their respective positions, and the second, mobile transmitter (TX1)

traversing a linear space from -0.2 m to 0.2 m with an offset of 0.0054 m. The results are in agreement with the theoretical values, notably the well-conditioned matrix and maximum channel capacity at the ideal position $d_{TX,ideal} = 0.0732\ m$ and at square-root integer multiples (i.e. $d_{TX,ideal} = \sqrt{\frac{nR*\lambda}{2}}$ where $n \in \mathbb{N}$) in Figure 4.1a and Figure 4.1b.
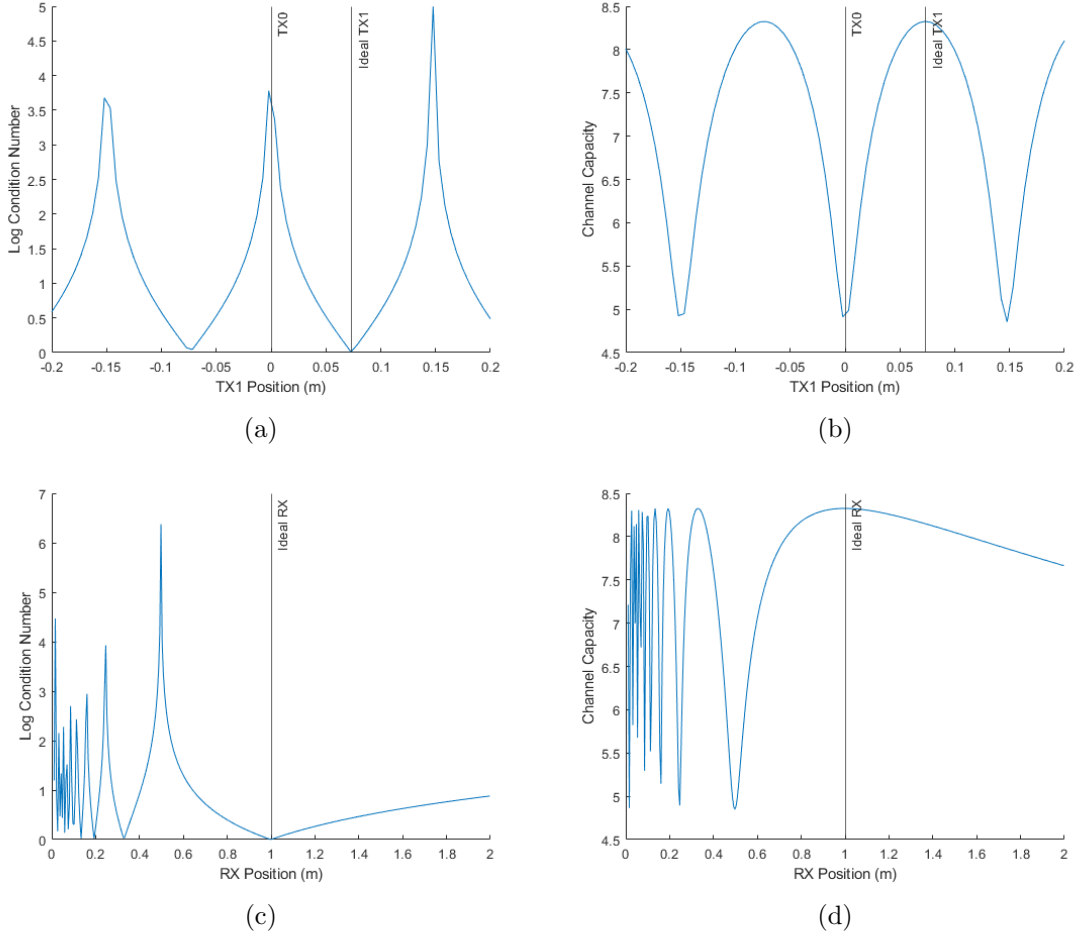
Figure 4.1: Theoretical values. From left to right, top to bottom: (a) condition number of the matrix as TX1 moves, (b) channel capacity of the matrix as TX1 moves, (c) condition number of the matrix as the ULA RX moves, and (d) channel capacity of the matrix as the ULA RX moves.

In the next validation check, the antenna spacings were fixed, but the distance between arrays is varied. Again, we confirm that we reach the maximum channel capacity and see

a well-conditioned matrix that agrees with the ideal positions from Rayleigh's criterion in Figure 4.1c and Figure 4.1d.

4.1.3   2x2 MIMO Moving TX1

Confident in the simulation model, a full coverage map was generated from -0.0732 m to 1.0732 m (width/x) by -0.0732 m to 0.1463 m (length/y), with the ULA phased arrays placed facing each other on the longer side of the map. At each offset position of the TX1, the signal would propagate directly to a reflector position at every $\delta x = \delta y = 0.0011m$ offset position, which would propagate the signal towards each of the receivers.

(a)   (b)

(c)   (d)
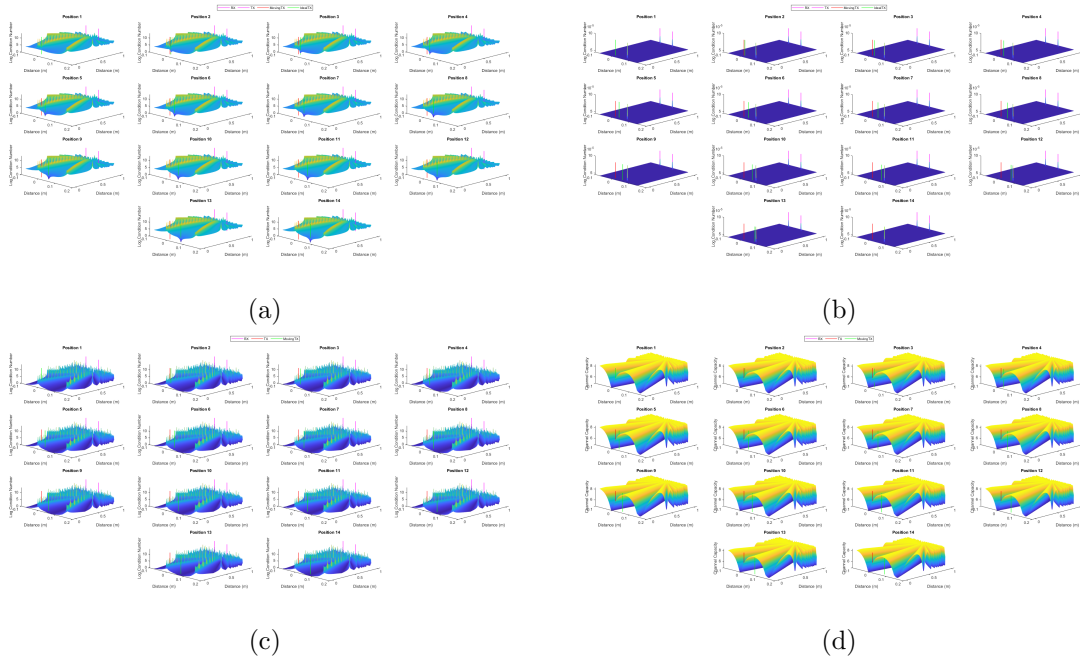
Figure 4.2: 2x2 NLoS MIMO simulation theoretical values as TX1 moves to 14 different positions. From left to right, top to bottom: (a) condition number of the matrix, (b) channel capacity of the matrix, (c) normalized condition number of the matrix, and (d) normalized channel capacity of the matrix.

Without any adjustments (Figure 4.2b, 4.2a), the results are as expected in that the LoS path (e.g. when the reflector is on top of TX1), the condition number is the lowest and the channel capacity is the highest due to the least amount of signal attenuation at that

position. Furthermore, the ideal position of TX1 produces the best condition number and the maximum channel capacity amongst all transmitter antenna spacing setups.

In the normalized simulated results (Figures 4.2d, 4.2c), we can distinctly see hyperbolic regions that are extremely ill-conditioned, areas that should be avoided when steering the phased arrays and define the boundaries of areas that produce well-conditioned, high capacity communication matrices. The results of the field are similar across all positions of antenna spacings, indicating that if an optimal power adjustment can be achieved, the placement of a scatter for a NLoS path is relatively simple if the given positions for the transmitter and receiver are known. The normalization process can be conducted with respective power adjustments on the transmitter side via pre-coding or a gain at the reflector using intelligent reflective surfaces (IRS) to equalize transmitted signals in assisting the selection of paths for the transmitter [27, 28, 16].

4.1.4   2x2 MIMO Moving RX ULA Array

The second investigated scenario places both transmitters and receivers at pre-defined offsets $(d_{TX,ideal} = 0.0732$ m) from the other transmitter and receiver. However, instead of having TX1 move, the RX ULA would move from $\lambda \approx 0.0107$ m away from the TX ULA to 1.5 m away. The coverage field spanned from -0.0732 m to 0.1463 m by -0.0732 m to 1.5 m, with the antenna array offset being $\delta R = 10\lambda = 0.1071$ m. The resulting condition number and channel capacity can be seen in Figure 4.3a and Figure 4.3b, respectively.

Here, we observe the hyperbolic regions emerge, albeit with less than desirable results compared to the case considering only the phase differences in Figures 4.3c and 4.3d. It can also be seen that the hyperbolic regions are centered heavily around the receiving antennas, indicating that the RX AP serves as the focal points for areas that produce orthogonal matrices.

(a)   (b)

(c)   (d)

Figure 4.3: 2x2 NLoS MIMO simulation theoretical values as RX moves from λ to $\frac{3R}{2}$. From left to right, top to bottom: (a) condition number of the matrix, (b) channel capacity of the matrix, (c) normalized condition number of the matrix, and (d) normalized channel capacity of the matrix.

4.1.5   3x3 MIMO Moving TX1

For the 3x3 MIMO case where one of the transmitters (TX1) linearly varies its position, the fixed transmitter antennas (TX0, TX2) were located at 0 m and $2 * d_{TX,ideal}$, where $d_{TX,ideal} = d_{RX,ideal} \approx 0.060$. The three receivers were placed at 0 m, $d_{RX,ideal}$, and $2 * d_{RX,ideal}$, respectively, and were situated 1 m away from the TX ULA. Under these conditions, the ideal position for TX1 were $d_{TX,ideal}$. The viewing port was from -0.0597 m to 0.1780 m by -0.0597 m to 1.5 m. The resulting condition number and channel capacity can be seen in Figures 4.4a and 4.4b.

Similar to the 2x2 NLoS MIMO, the LoS path was significantly better in both metrics compared to other areas. Aside from the LoS path, other regions that provided noticeable improvement in the channel capacity and were comparably well-conditioned was when the

reflectors were on top of the receivers. Eliminating the gain, we observe the same hyperbolic form dictating excellent positions for the scatter in Figures 4.4c and 4.4d.

(a)

(b)

(c)

(d)
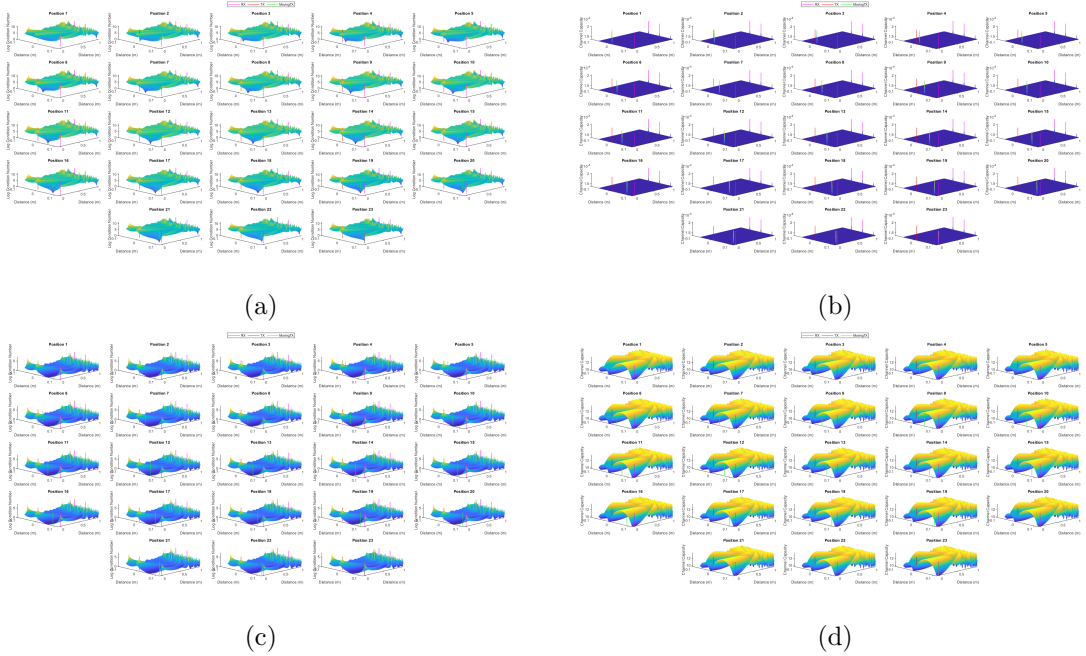
Figure 4.4: 3x3 NLoS MIMO simulation theoretical values as TX1 moves to 18 different positions. From left to right, top to bottom: (a) condition number of the matrix, (b) channel capacity of the matrix, (c) normalized condition number of the matrix, and (d) normalized channel capacity of the matrix.

4.1.6 3x3 MIMO Moving RX ULA Array

The final simulated scenario places both transmitters and receivers at pre-defined offsets ($d_{TX,ideal} = 0.060$ m) from the other transmitters and receivers. The RX ULA would move from $\lambda \approx 0.0107$ m away from the TX ULA to 1.5 m away. The coverage field spanned from -0.0597 m to 0.1780 m by -0.0597 m to 1.5 m, with the antenna array offset being $\delta R = 10\lambda = 0.1071$ m. The resulting condition number and channel capacity can be seen in Figure 4.5a and Figure 4.5b, respectively.

From these figures, we can see that, as opposed to the 2x2 MIMO situation, the hyperbolic regions transform around the receivers in a honeycomb-like pattern before branching out in the defined hyperbolic shape. This provides insight into the idea that,

when scaling antenna elements in a mmWave MIMO, the positions near the receiver elements through the NLoS path begin to collide with hyberbolic regions from the additional antennas. This is further highlighted as we focus on the phase effects in Figures 4.5c and 4.5d.
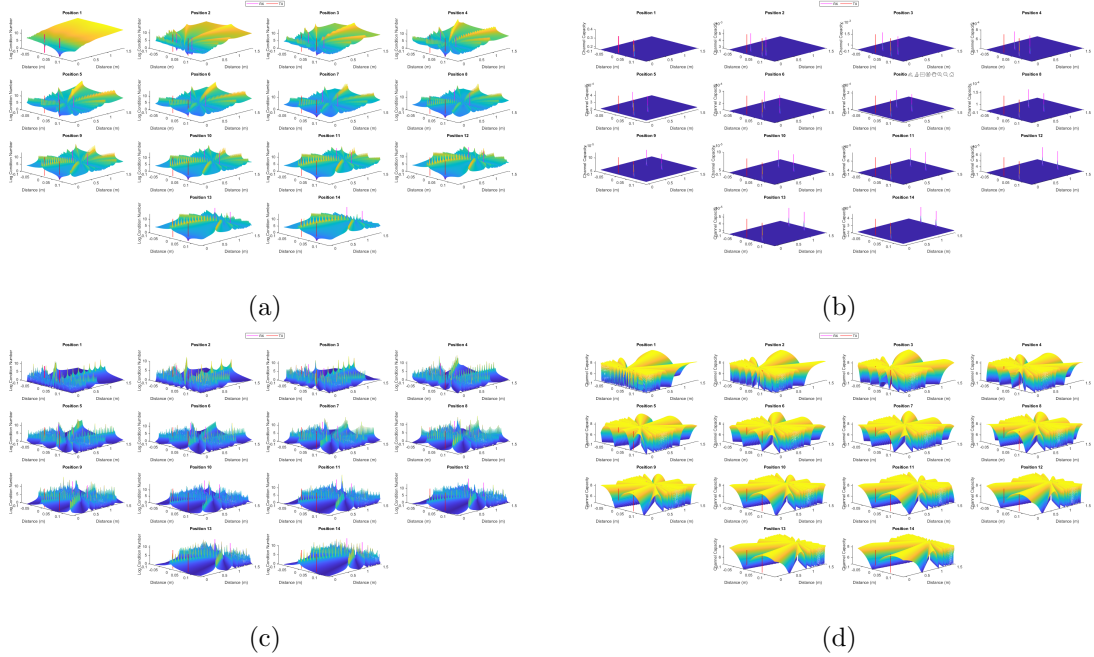

(a)

(b)

(c)

(d)
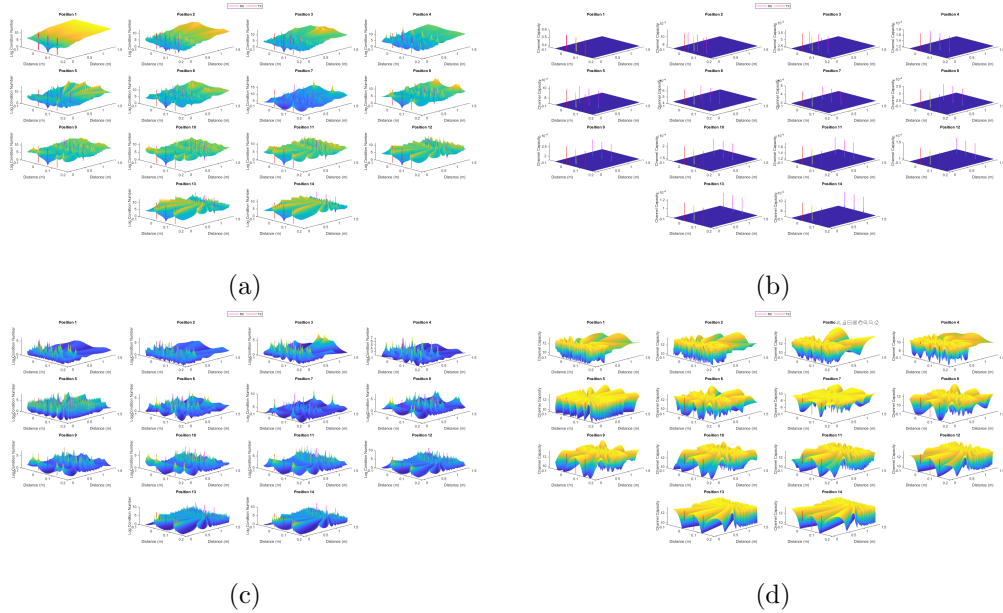
Figure 4.5: 3x3 NLoS MIMO simulation theoretical values as RX moves from λ to $\frac{3R}{2}$. From left to right, top to bottom: (a) condition number of the matrix, (b) channel capacity of the matrix, (c) normalized condition number of the matrix, and (d) normalized channel capacity of the matrix.

4.2 Testbed Measurements

The following subsections discuss the setup of the real-life measurements for LoS and NLoS mmWave MIMO explored and an analysis comparing the results to the simulations and to each other.

4.2.1 Setup

For the real-life experiments, we mimic the MIMO channel matrix in a similar fashion as the simulation. With the limitations of having only two beamformers capable of operating

at the mmWave band, we take channel measurements between the transmitter and receivers at positions where they would be under a MIMO system with ULA antennas.

The measurements are assembled for the resulting matrix and corresponding analysis of the channel capacity and condition number. With the NLoS path, the reflector was placed 0.743 m away equidistant from the transmitter at 0 m and the receiver at 0 m parallel to the LoS between the two APs. The transmitter and the receiver were steered at a 45 degree and -45 degree angle, respectively. There were 100 measurements for each trace, which were averaged together for the final analysis. An example for the LoS and NLoS path can be seen in Figure 4.6.
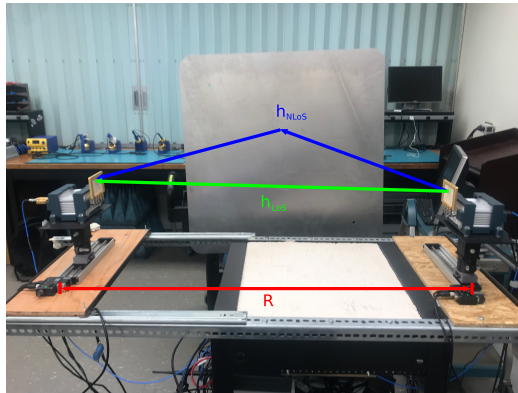
Figure 4.6: Real-life mmWave measurement paths.

4.2.2 Transmission Power

Table 4.1: Power measurements.

	Power (dBm)
Transmitted Power	-20
Received Power	-63
Received Power After Power Splitter	-60
Link Budget	-40

32

To properly gauge the power consumption of the testbed, the transmitted and received signal powers were measured using a spectrum analyzer. Splitting the signal using a power splitter at both ends, at the egress of the FieldFox was -20 dBm and the power at the entry at port 2 was -63 dBm. Factoring in the 3 dB drop from the power splitter, the effective link budget for the system was approximately -40 dB. This loss is a combination of various elements within the system including UD Box insertion loss, cable loss, environment path fading, and active antenna gains. The breakdown of the link budget power losses can be seen in Table 4.2.

Table 4.2: Link budget derivatives.

	Power Loss (dB)
Up/Down Converter	-9
TX Gain/Return Loss	+25/-10
RX Gain/Return Loss	+10/-10
Channel Loss	-26
COM Port Loss	-7
Cable Loss	-1
Power Splitter	-3

4.2.3   2x2 MIMO, R = 1.0 m

In the LoS measurements where the distance between the transmitter and receivers were 1.0 m, the RX beamformer was fixed at two locations: 0 mm and 70 mm. The TX beamformer moved in 10 mm increments from 0 mm to 70 mm. At each instance, the linear magnitude and phase collected from the FieldFox were transformed into the CSI. Measurements from the TX at the 0 mm position to the 0 mm RX and the 70 mm RX were used as h_{11} and h_{12}, respectively, and measurements from the moving TX to the 0 mm RX and the 70 mm RX were used as h_{21} and h_{22}, respectively. The average SNR was approximately 26 dB.

Despite a fixed direction for each TX1 position, we can see that the condition number is relatively well-conditioned for every position below 40 mm with a slight decrease in channel capacity compared to the optimal LoS matrix. This means that despite the

Figure 4.7: Moving TX combined LoS and NLoS measurements at R = 1 m. From left to right, top to bottom: (a) channel capacity, (b) condition number, (c) normalized channel capacity, and (d) normalized condition number.

suboptimal directionality of the beam, it is possible to obtain near optimal results. As is, the values for the channel capacity for the LoS were about 0.182, a trend that was mimicked for the NLoS measurements, but at 0.1. The condition number for the LoS channel capacity begins to show signs of similarity to the theoretical expectation, and the NLoS condition number remained around 10^2, indicating ill-conditioned channel matrices. After power optimization, these computed values match the theory and simulation results, demonstrating how aberrations to the optimal antenna spacing result in ill-conditioned matrices for the LoS. In the NLoS, we see a significant improvement in the channel capacity,

having results within 5% of the channel capacity at the ideal position for the LoS case. Similarly, for the condition numbers, the LoS is in well-agreement with the theory, and the NLoS positions have a condition number less than 10 for every position below 40 mm. This demonstrates the capability of maintaining relatively decent communication links in confined transmitter spaces by utilizing NLoS paths.
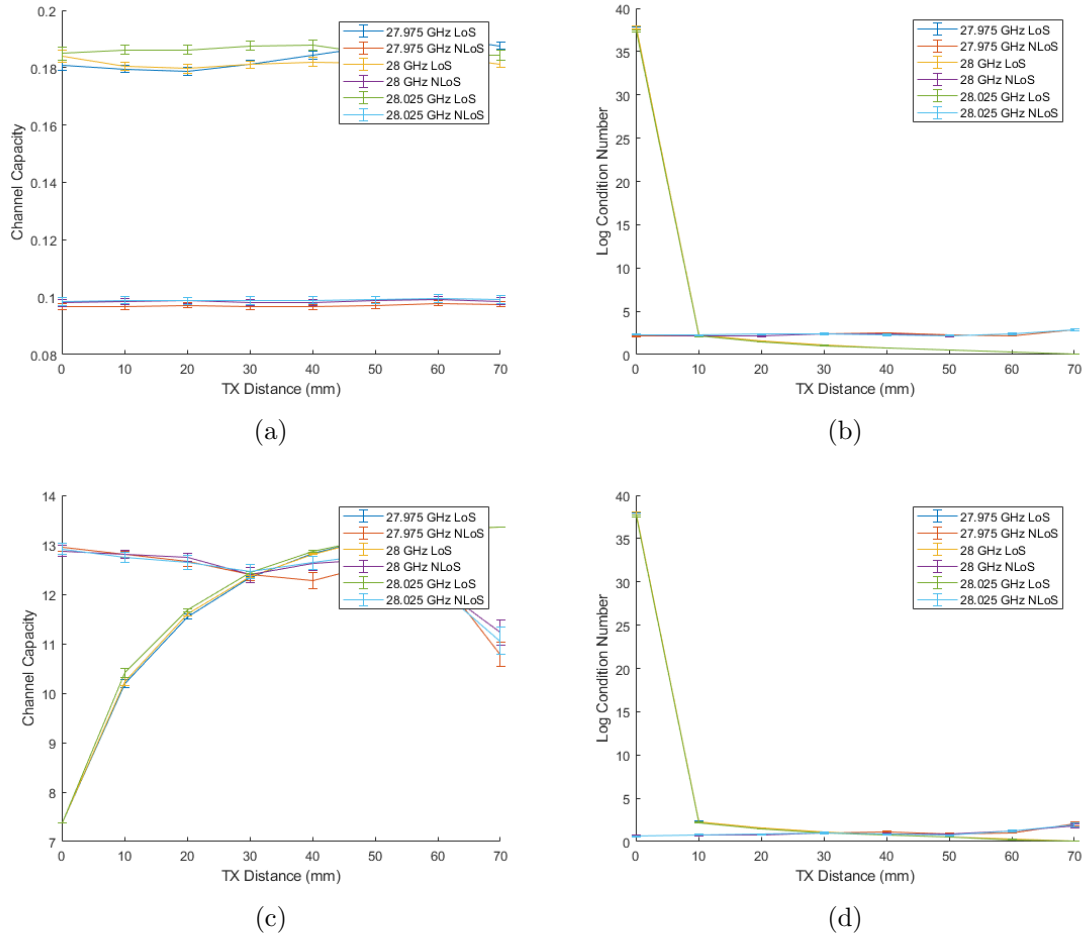
4.2.4   2x2 MIMO, R = 1.2 m
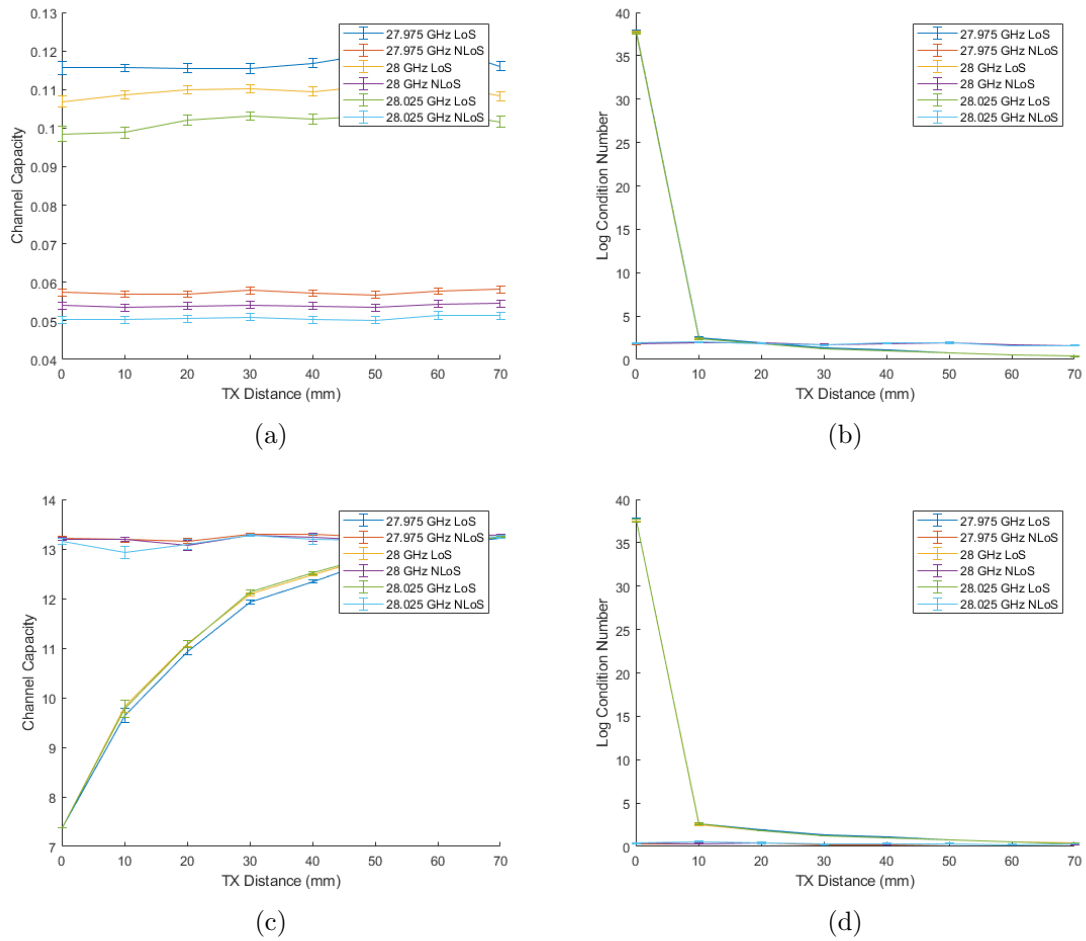

Figure 4.8: Moving TX combined LoS and NLoS measurements at R = 1.2 m. From left to right, top to bottom: (a) channel capacity, (b) condition number, (c) normalized channel capacity, and (d) normalized condition number.

At the longer range measurements, the positions of the receivers were placed at $R = 1.2$ m. For this setup, TX1 is moved from 0 mm to 70 mm in with $\delta x = 10\ mm$ and the measurement procedure is similar the the 2x2 MIMO measurements.

In the same fashion as the previous measurements, we see in the typical case without any adjustment higher channel capacities in the LoS situations compared to the NLoS, but overal lower channel capacities as we break outside of the ideal distance between antenna arrays (e.g. 1 m) (Figures 4.8a and 4.8b). This is reiterated in the condition numbers. Analyzing the phase differences, the channel capacities for the NLoS case improves even further, with only a 0.5% drop from the channel capacity at the ideal LoS position from all TX1 positions (Figure 4.3d). The condition numbers for the NLoS paths drop even further to below 3 (Figure 4.3c). The reason for these differences compared to when R = 1 m is most likely attributed to the imprecise reflection and angles of the given setup. Regardless, these results demonstrate the ability of enhancing the communication link through NLoS paths when the LoS path is not available and, even more importantly, can be used to reduce the antenna spacing.

4.3   Related Work

Relevant literature in regards to mmWave MIMO focuses heavily on the LoS paths [13, 14, 27, 28] and massive MIMO antenna elements [11, 12]. However, these works don't focus on leveraging solely NLoS paths, seeking to exploit multiple solutions of Rayleigh criterion to stretch the boundaries of optimum antenna spacing as much as possible, either physically or through antenna array reconfigurations. Other works leverage the NLoS link as a method to augment the LoS path [29, 30] or to isolate the positioning of the transmitted beam for a LoS connection [9, 31, 32]. Again, we see the propensity towards the LoS link, a contrast to the NLoS approach conducted in this work.

Chapter 5

Conclusion and Future Work

In this section, we conclude the paper with a summary of the work done and the significance of the work. Future work to be explored to extend the work done is also presented.

5.1 Conclusion

In this report, simulations of the 2x2 MIMO and 3x3 MIMO channel environment when one of the transmitters uses solely a NLoS path was presented, providing the condition number and channel capacity at each offset instance. Real-world measurements were conducted at two different antenna array spacings and at mmWave frequencies to verify the LoS theory on optimal spacing as well as to identify the ability to use NLoS paths to break-free from the spatial constraints guided by the Rayleigh criterion. Such experiments confirmed the ability to do so and vindicated the potential for said multipaths to also be used when the distance between transmitters and receivers are longer. The preliminary research results in this paper provide a foundation for further research and optimization, making use of NLoS paths at the n257 band to allow smaller dimensions in transmitter spacing. The provided results can serve as guidelines for leveraging NLoS mmWave MIMO for V2V and other compact designs.

5.2   Future Work

These preliminary efforts focused on a proof-of-concept and can be extended in numerous ways. Such possibilities include actual testing of mentioned algorithms, investigation into 2-dimensional spacing phased arrays to further reduce the space occupied by antennas, and a 3-dimensional coverage map to analyze the impacts of artifacts including, but not limited to, walls, ceilings, and floors.

Bibliography

[1] J. Clement. *Global Mobile Traffic 2022*. July 2022. URL: `https://www.statista.com/statistics/277125/share-of-website-traffic-coming-from-mobile-devices/`.

[2] 3GPP. *5G Technical Specifications and Technical Reports for a 5G based 3GPP system*. Technical Specification (TS) 21.205. Version 15.0.0. 3rd Generation Partnership Project (3GPP), Apr. 2018. URL: `https://www.etsi.org/deliver/etsi_TS/121200_121299/121205/15.00.00_60/ts_121205v150000p.pdf`.

[3] Wonil Roh et al. "Millimeter-wave beamforming as an enabling technology for 5G cellular communications: theoretical feasibility and prototype results". In: *IEEE Communications Magazine* 52.2 (2014), pp. 106–113. DOI: `10.1109/MCOM.2014.6736750`.

[4] Dingyou Ma et al. "Joint Radar-Communication Strategies for Autonomous Vehicles: Combining Two Key Automotive Technologies". In: *IEEE Signal Processing Magazine* 37.4 (2020), pp. 85–97. DOI: `10.1109/MSP.2020.2983832`.

[5] David Tse and Pramod Viswanath. *Fundamentals of Wireless Communication*. USA: Cambridge University Press, 2005. ISBN: 0521845270.

[6] Oussama Souihli and Tomoaki Ohtsuki. "Benefits of Rich Scattering in MIMO Channels: A Graph-Theoretical Perspective". In: *IEEE Communications Letters* 17.1 (2013), pp. 23–26. DOI: `10.1109/LCOMM.2012.120312.121184`.

[7] Hao Zhou, Dongning Guo, and Michael L. Honig. "Beam Acquisition and Training in Millimeter Wave Networks With Narrowband Pilots". In: *IEEE Journal on Selected Areas in Communications* 37.12 (2019), pp. 2759–2771. DOI: `10.1109/JSAC.2019.2947856`.

[8] Ahmed Al-Saman et al. "Survey of Millimeter-Wave Propagation Measurements and Models in Indoor Environments". In: *Electronics* 10.14 (2021). ISSN: 2079-9292. DOI: `10.3390/electronics10141653`. URL: `https://www.mdpi.com/2079-9292/10/14/1653`.

[9] Alejandro Blanco et al. "Augmenting MmWave Localization Accuracy through Sub-6 GHz on off-the-Shelf Devices". In: *Proceedings of the 20th Annual International Conference on Mobile Systems, Applications and Services*. MobiSys '22. Portland, Oregon: Association for Computing Machinery, 2022, pp. 477–490. ISBN: 9781450391856. DOI: `10.1145/3498361.3538920`. URL: `https://doi.org/10.1145/3498361.3538920`.

[10] 2019. URL: `https://cdn.brandfolder.io/D8DI15S7/as/qcra3r-2jik60-cze57x/mmWave-Networks_Study-of-mmWave-Signal-Propagation-in-Non-line-of-site-Environment_-_White_Paper_-_Telecom_Infra_Project.pdf`.

[11] Thomas L. Marzetta. "Massive MIMO: An Introduction". In: *Bell Labs Technical Journal* 20 (2015), pp. 11–22. DOI: `10.15325/BLTJ.2015.2407793`.

[12] Stefano Buzzi and Carmen D'Andrea. *Massive MIMO 5G Cellular Networks: mm-wave vs. μ-wave Frequencies*. 2017. DOI: `10.48550/ARXIV.1702.07187`. URL: `https://arxiv.org/abs/1702.07187`.

[13] Akbar M. Sayeed and Vasanthan Raghavan. "Maximizing MIMO Capacity in Sparse Multipath With Reconfigurable Antenna Arrays". In: *IEEE Journal of Selected Topics in Signal Processing* 1.1 (2007), pp. 156–166. DOI: `10.1109/JSTSP.2007.897057`.

[14] Mario H. Castañeda Garcia, Marcin Iwanow, and Richard A. Stirling-Gallacher. "LOS MIMO Design Based on Multiple Optimum Antenna Separations". In: *2018 IEEE*

88th Vehicular Technology Conference (VTC-Fall). 2018, pp. 1–5. DOI: `10.1109/ VTCFall.2018.8690668`.

[15] Eric Torkildson, Hong Zhang, and Upamanyu Madhow. "Channel modeling for millimeter wave MIMO". In: *2010 Information Theory and Applications Workshop (ITA)*. 2010, pp. 1–8. DOI: `10.1109/ITA.2010.5454109`.

[16] John Nolan, Kun Qian, and Xinyu Zhang. "RoS: Passive Smart Surface for Roadside-to-Vehicle Communication". In: *Proceedings of the 2021 ACM SIGCOMM 2021 Conference*. SIGCOMM '21. Virtual Event, USA: Association for Computing Machinery, 2021, pp. 165–178. ISBN: 9781450383837. DOI: `10.1145/3452296. 3472896`. URL: `https://doi.org/10.1145/3452296.3472896`.

[17] Qiong He, Shulin Sun, and Lei Zhou. "Tunable/Reconfigurable Metasurfaces: Physics and Applications". In: *Research* 2019 (July 2019), pp. 1–16. DOI: `10.34133/2019/ 1849272`.

[18] Qingqing Wu et al. *Intelligent Reflecting Surface Aided Wireless Communications: A Tutorial*. 2020. DOI: `10.48550/ARXIV.2007.02759`. URL: `https://arxiv.org/abs/ 2007.02759`.

[19] Manideep Dunna et al. "ScatterMIMO: Enabling Virtual MIMO with Smart Surfaces". In: *Proceedings of the 26th Annual International Conference on Mobile Computing and Networking*. MobiCom '20. London, United Kingdom: Association for Computing Machinery, 2020. ISBN: 9781450370851. DOI: `10.1145/3372224.3380887`. URL: `https://doi.org/10.1145/3372224.3380887`.

[20] B.E. Henty and D.D. Stancil. "Bandwidth limitations of phase-conjugate arrays used for multipath focusing". In: *IEEE Antennas and Propagation Society Symposium, 2004*. Vol. 3. 2004, 2792–2795 Vol.3. DOI: `10.1109/APS.2004.1331955`.

[21] Tim Halsig et al. "Measurement Results for Millimeter Wave Pure LOS MIMO Channels". In: *2017 IEEE Wireless Communications and Networking Conference (WCNC)*. 2017, pp. 1–6. DOI: `10.1109/WCNC.2017.7925749`.

[22] Lei Bao and Bengt-Erik Olsson. "Methods and measurements of channel phase difference in 2×2 microwave LOS-MIMO systems". In: *2015 IEEE International Conference on Communications (ICC)* (2015), pp. 1358–1363.

[23] Yasaman Ghasempour et al. "Multi-Stream Beam-Training for MmWave MIMO Networks". In: *Proceedings of the 24th Annual International Conference on Mobile Computing and Networking*. MobiCom '18. New Delhi, India: Association for Computing Machinery, 2018, pp. 225–239. ISBN: 9781450359030. DOI: 10.1145/3241539.3241556. URL: https://doi.org/10.1145/3241539.3241556.

[24] Xiufeng Xie et al. "Hekaton: Efficient and Practical Large-Scale MIMO". In: *Proceedings of the 21st Annual International Conference on Mobile Computing and Networking*. MobiCom '15. Paris, France: Association for Computing Machinery, 2015, pp. 304–316. ISBN: 9781450336192. DOI: 10.1145/2789168.2790116. URL: https://doi.org/10.1145/2789168.2790116.

[25] Suraj Jog et al. "Many-to-Many Beam Alignment in Millimeter Wave Networks". In: *Proceedings of the 16th USENIX Conference on Networked Systems Design and Implementation*. NSDI'19. Boston, MA, USA: USENIX Association, 2019, pp. 783–800. ISBN: 9781931971492.

[26] S. Khanna and K. Kumaran. "On wireless spectrum estimation and generalized graph coloring". In: *Proceedings. IEEE INFOCOM '98, the Conference on Computer Communications. Seventeenth Annual Joint Conference of the IEEE Computer and Communications Societies. Gateway to the 21st Century (Cat. No.98*. Vol. 3. 1998, 1273–1283 vol.3. DOI: 10.1109/INFCOM.1998.662942.

[27] Mojtaba Ahmadi Almasi et al. "A New Reconfigurable Antenna MIMO Architecture for mmWave Communication". In: *2018 IEEE International Conference on Communications (ICC)*. 2018, pp. 1–7. DOI: 10.1109/ICC.2018.8422414.

[28] Wahaj Abbas Awan et al. "Frequency Reconfigurable patch antenna for millimeter wave applications". In: *2019 2nd International Conference on Computing,*

Mathematics and Engineering Technologies (iCoMET). 2019, pp. 1–5. DOI: 10.1109/ ICOMET.2019.8673417.

[29] Rico Mendrzik et al. "Harnessing NLOS Components for Position and Orientation Estimation in 5G Millimeter Wave MIMO". In: *IEEE Transactions on Wireless Communications* 18.1 (2019), pp. 93–107. DOI: 10.1109/TWC.2018.2877615.

[30] Ish Kumar Jain, Raghav Subbaraman, and Dinesh Bharadia. "Two Beams Are Better than One: Towards Reliable and High Throughput MmWave Links". In: *Proceedings of the 2021 ACM SIGCOMM 2021 Conference*. SIGCOMM '21. Virtual Event, USA: Association for Computing Machinery, 2021, pp. 488–502. ISBN: 9781450383837. DOI: 10.1145/3452296.3472924. URL: https://doi.org/10.1145/3452296.3472924.

[31] Chen Huang et al. "Machine Learning-Enabled LOS/NLOS Identification for MIMO Systems in Dynamic Environments". In: *IEEE Transactions on Wireless Communications* 19.6 (2020), pp. 3643–3657. DOI: 10.1109/TWC.2020.2967726.

[32] Chiehping Lai et al. "Methodology for Multipath-Component Tracking in Millimeter-Wave Channel Modeling". en. In: 67 (Mar. 2019). DOI: https://doi.org/10.1109/ TAP.2018.2888686. URL: https://tsapps.nist.gov/publication/get_pdf.cfm? pub_id=925050.

Appendix A

simulation.m

```matlab
1   clear all; close all; clc;
2   tic
3   %% setup
4   filename = "2x2_los";
5
6   cfreq = 28e9;
7   bw = 1e6;
8   c = 2.997925e8;
9   lambda = c / cfreq;
10  R = 1;
11  dTRX = sqrt(R*lambda/2);
12
13  tx = [[0;0;0],...
14       [0;dTRX;0]];
15  vel1 = zeros(3, 1);
16
17  rx = [[R;0;0],...
18       [R;dTRX;0]];
19  vel2 = zeros(size(rx));
20
21  viewbox = [-dTRX R+dTRX; ...      % x-axis
22             -dTRX 2*dTRX];              % z-axis
23
24  signal = ones(1,length(rx(1,:)));
```

```matlab
25
26  %% simulation
27  henv = phased.FreeSpace('SampleRate',8e3,...
28      'OperatingFrequency',cfreq);
29
30  allH = [];
31  for txMoveVert = tx(2,1):lambda/2:tx(2,2)
32      fH = [];
33
34      for col=viewbox(1,1):lambda/10:viewbox(1,2)
35          colH = [];
36
37          iterateArr = viewbox(2,1):lambda/10:viewbox(2,2);
38          parfor i=1:length(iterateArr)
39              H = [];
40
41              y = step(henv,...
42                  signal,...
43                  tx(:,1),...
44                  rx,...
45                  vel1,...
46                  vel2);
47              henv.release();
48              H = [H; y];
49
50              r = step(henv,...
51                  1,...
52                  [0;txMoveVert;0],...
53                  [col + lambda/1000;iterateArr(i);0],...
54                  vel1,...
55                  vel1);
56              henv.release();
57
58              r = step(henv,...
59                  [r r],...
60                  [col + lambda/1000;iterateArr(i);0],...
61                  rx,...
```

45

```matlab
62                    vel1,...
63                    vel2);
64                henv.release();
65                    H = [H; r];
66
67                colH = [colH H];
68            end
69            fH = [fH; colH];
70        end
71        allH = cat(3, allH, fH);
72 end
73
74 toc
75 save(filename + ".mat");
```

Appendix B

plot_all.m

```matlab
clear all; clc;

%% initialize
load('data.mat')

dim = size(allH);

SNR = 15; % dB
movingTXSpacing = lambda/2;
XSpacing = lambda/10;
YSpacing = lambda/10;

allH = allH./abs(allH);
[X,Y] = meshgrid(viewbox(2):XSpacing:viewbox(4),...
                 viewbox(1):YSpacing:viewbox(3));

%% cond num
figure(1);
tiledlayout(4,4);

for i=1:dim(3)
    if i == 13
        nexttile
    end
```

```matlab
        condNum = [];
        for k=1:2:dim(1)
            rowCap = []; rowNum = [];
            for j=1:2:dim(2)
                vect = allH(k:k+1,j:j+1,i);
                rowNum = [rowNum log(cond(vect))];
            end
            condNum = [condNum; rowNum];
        end

        movingTX = tx(4) + movingTXSpacing*(i-1);


        nexttile
        hold on
        Z = condNum;
        topBoundary = max(max(Z));
        botBoundary = min(min(Z));

        % fixed
        plot3([rx(2) rx(2)],[rx(1) rx(1)],[botBoundary topBoundary],...
            'Color','m','LineWidth',1)

        plot3([tx(2) tx(2)],[tx(1) tx(1)],[botBoundary topBoundary],...
            'Color','r','LineWidth',1)

        % moving
        plot3([movingTX movingTX],[tx(1) tx(1)],[botBoundary topBoundary],...
            'Color','g','LineWidth',1)
        mesh(X,Y,Z)

        plot3([rx(5) rx(5)],[rx(4) rx(4)],[botBoundary topBoundary],...
            'Color','m','LineWidth',1)

        % labels
        title('Position ' + string(i))
        xlabel('Distance (m)')
```

```matlab
62        ylabel('Distance (m)')
63        zlabel('Log Condition Number')
64        view(45,45)
65        hold off
66    end
67    delete(nexttile(13))
68
69    leg = legend({'RX', 'TX', 'MovingTX'},...
70        'Location','NorthOutside','Orientation','Horizontal');
71    leg.Layout.Tile = 'North';
72
73    %% chan cap
74    figure(2);
75    tiledlayout(4,4);
76
77    for i=1:dim(3)
78        if i == 13
79            nexttile
80        end
81
82        chanCap = [];
83        for k=1:2:dim(1)
84            rowCap = [];
85            for j=1:2:dim(2)
86                vect = allH(k:k+1,j:j+1,i);
87                rowCap = [rowCap log(det(eye(2)+(10^(SNR/10))*(vect*vect')))];
88            end
89            chanCap = [chanCap; rowCap];
90        end
91
92        movingTX = tx(4) + movingTXSpacing*(i-1);
93
94        nexttile
95        hold on
96        Z = abs(chanCap);
97        topBoundary = max(max(Z));
98        botBoundary = min(min(Z));
```

```matlab
99
100        % fixed
101        plot3([rx(2) rx(2)],[rx(1) rx(1)],[botBoundary topBoundary],...
102            'Color','m','LineWidth',1)
103
104        plot3([tx(2) tx(2)],[tx(1) tx(1)],[botBoundary topBoundary],...
105            'Color','r','LineWidth',1)
106
107        % moving
108        plot3([movingTX movingTX],[tx(1) tx(1)],[botBoundary topBoundary],...
109            'Color','g','LineWidth',1)
110        mesh(X,Y,Z)
111
112        plot3([rx(5) rx(5)],[rx(4) rx(4)],[botBoundary topBoundary],...
113            'Color','m','LineWidth',1)
114
115        % labels
116        title('Position ' + string(i))
117        xlabel('Distance (m)')
118        ylabel('Distance (m)')
119        zlabel('Channel Capacity')
120        view(45,45)
121        hold off
122    end
123    delete(nexttile(13))
124
125    leg = legend({'RX', 'TX', 'MovingTX'},...
126            'Location','NorthOutside','Orientation','Horizontal');
127    leg.Layout.Tile = 'North';
```

Appendix C

process_experiment_data.m

```matlab
clear all; close all; clc;

%% LoS
result = [];
filepath = "Data\\Path";

for i=0:10:70
    load(filepath + "\\los\\rx0\\tx0_rx0.mat");
    h11 = csi;
    result(1:2:6,1:2:200,(i/10)+1) = h11;

    load(filepath + "\\los\\rx70\\tx0_rx70.mat");
    h12 = csi;
    result(1:2:6,2:2:200,(i/10)+1) = h12;

    load(filepath + "\\los\\rx0\\tx" + string(i) + "_rx0.mat");
    h21 = csi;
    result(2:2:6,1:2:200,(i/10)+1) = h21;

    load(filepath + "\\los\\rx70\\tx" + string(i) + "_rx70.mat");
    h22 = csi;
    result(2:2:6,2:2:200,(i/10)+1) = h22;
end
```

```matlab
25    result = result./abs(result);
26
27    SNR = 26;
28    los_cond_num = [];
29    los_chan_cap = [];
30    for i=1:8
31        for j=1:2:6
32            for k=1:2:200
33                vect = result(j:j+1,k:k+1,i);
34                los_cond_num(ceil(j/2),ceil(k/2),i) = cond(vect);
35                los_chan_cap(ceil(j/2),ceil(k/2),i) = ...
36                    log(det(eye(2) + (10^(SNR/10)) * (vect*vect')));
37            end
38        end
39    end
40
41    %% NLoS
42    filepath = "C:\\Users\\Willy\\Desktop\\R1.2_new";
43    for i=0:10:70
44        load(filepath + "\\los\\rx0\\tx0_rx0.mat");
45        h11 = csi;
46        result(1:2:6,1:2:200,(i/10)+1) = h11;
47
48        load(filepath + "\\los\\rx70\\tx0_rx70.mat");
49        h12 = csi;
50        result(1:2:6,2:2:200,(i/10)+1) = h12;
51
52        load(filepath + "\\nlos\\rx0\\tx" + string(i) + "_rx0.mat");
53        h21 = csi;
54        result(2:2:6,1:2:200,(i/10)+1) = h21;
55
56        load(filepath + "\\nlos\\rx70\\tx" + string(i) + "_rx70.mat");
57        h22 = csi;
58        result(2:2:6,2:2:200,(i/10)+1) = h22;
59    end
60
61    result = result./abs(result);
```

```matlab
62
63  SNR = 26;
64  nlos_cond_num = [];
65  nlos_chan_cap = [];
66  for i=1:8
67      for j=1:2:6
68          for k=1:2:200
69              vect = result(j:j+1,k:k+1,i);
70              nlos_cond_num(ceil(j/2),ceil(k/2),i) = cond(vect);
71              nlos_chan_cap(ceil(j/2),ceil(k/2),i) = ...
72                  log(det(eye(2) + (10^(SNR/10)) * (vect*vect')));
73          end
74      end
75  end
76
77  %% plot
78  X = 0:10:70;
79  freqs = 27.975:0.025:28.025;
80
81  figure(1)
82  hold on
83  for i=1:3
84      log_cond = log(los_cond_num(i,:,:));
85      avg = reshape(mean(log_cond), [1 8]);
86      SEM = reshape(std(log_cond)./sqrt(100), [1 8]);
87      CI = SEM * tinv(0.975, 99);
88      errorbar(X, avg, CI, 'DisplayName', string(freqs(i)) + " GHz LoS")
89
90      log_cond = log(nlos_cond_num(i,:,:));
91      avg = reshape(mean(log_cond), [1 8]);
92      SEM = reshape(std(log_cond)./sqrt(100), [1 8]);
93      CI = SEM * tinv(0.975, 99);
94      errorbar(X, avg, CI, 'DisplayName', string(freqs(i)) + " GHz NLoS")
95  end
96  xlabel("TX Distance (mm)")
97  ylabel("Log Condition Number")
98  legend()
```

```matlab
99   hold off
100
101  figure(2)
102  hold on
103  for i=1:3
104      abs_cap = abs(los_chan_cap(i,:,:));
105      avg = reshape(mean(abs_cap), [1 8]);
106      SEM = reshape(std(abs_cap)./sqrt(100), [1 8]);
107      CI = SEM * tinv(0.975, 99);
108      errorbar(X, avg, CI, 'DisplayName', string(freqs(i)) + " GHz LoS")
109
110      abs_cap = abs(nlos_chan_cap(i,:,:));
111      avg = reshape(mean(abs_cap), [1 8]);
112      SEM = reshape(std(abs_cap)./sqrt(100), [1 8]);
113      CI = SEM * tinv(0.975, 99);
114      errorbar(X, avg, CI, 'DisplayName', string(freqs(i)) + " GHz NLoS")
115  end
116  xlabel("TX Distance (mm)")
117  ylabel("Channel Capacity")
118  legend()
119  hold off
120
121  figure(3)
122  hold on
123  log_cond = log(los_cond_num(2,:,:));
124  avg = reshape(mean(log_cond), [1 8]);
125  SEM = reshape(std(log_cond)./sqrt(100), [1 8]);
126  CI = SEM * tinv(0.975, 99);
127  errorbar(X, avg, CI, 'DisplayName', "28 GHz LoS")
128
129  log_cond = log(nlos_cond_num(2,:,:));
130  avg = reshape(mean(log_cond), [1 8]);
131  SEM = reshape(std(log_cond)./sqrt(100), [1 8]);
132  CI = SEM * tinv(0.975, 99);
133  errorbar(X, avg, CI, 'DisplayName', "28 GHz LoS")
134  xlabel("TX Distance (mm)")
135  ylabel("Log Condition Number")
```

```matlab
136  legend()
137  hold off
138
139  figure(4)
140  hold on
141  abs_cap = abs(los_chan_cap(2,:,:));
142  avg = reshape(mean(abs_cap), [1 8]);
143  SEM = reshape(std(abs_cap)./sqrt(100), [1 8]);
144  CI = SEM * tinv(0.975, 99);
145  errorbar(X, avg, CI, 'DisplayName', "28 GHz LoS")
146
147  abs_cap = abs(nlos_chan_cap(2,:,:));
148  avg = reshape(mean(abs_cap), [1 8]);
149  SEM = reshape(std(abs_cap)./sqrt(100), [1 8]);
150  CI = SEM * tinv(0.975, 99);
151  errorbar(X, avg, CI, 'DisplayName', "28 GHz NLoS")
152  xlabel("TX Distance (mm)")
153  ylabel("Channel Capacity")
154  legend()
155  hold off
```